

## Article

# Effect of Traps on the UV Sensitivity of Gallium Oxide-Based Structures

Vera M. Kalygina <sup>1,\*</sup>, Alexander V. Tsymbalov <sup>1</sup> , Petr M. Korusenko <sup>2,3</sup> , Aleksandra V. Koroleva <sup>4</sup>  
and Evgeniy V. Zhizhin <sup>4</sup> 

<sup>1</sup> Research and Development Centre for Advanced Technologies in Microelectronics, National Research Tomsk State University, 634050 Tomsk, Russia; zoldmine@gmail.com

<sup>2</sup> Department of Solid State Electronics, Saint Petersburg State University, 199034 Saint Petersburg, Russia; korusenko\_petr@mail.ru

<sup>3</sup> Department of Physics, Omsk State Technical University, 644050 Omsk, Russia

<sup>4</sup> Research Park, Saint Petersburg State University, 199034 Saint Petersburg, Russia; koroleva.alexandra.22@gmail.com (A.V.K.); evgeny\_liquid@mail.ru (E.V.Z.)

\* Correspondence: vmkalygina@mail.ru

**Abstract:** Resistive metal/ $\beta$ -Ga<sub>2</sub>O<sub>3</sub>/metal structures with different interelectrode distances and electrode topologies were investigated. The oxide films were deposited by radio-frequency magnetron sputtering of a Ga<sub>2</sub>O<sub>3</sub> (99.999%) target onto an unheated sapphire c-plane substrate (0001) in an Ar/O<sub>2</sub> gas mixture. The films are sensitive to ultraviolet radiation with wavelength  $\lambda = 254$ . Structures with interdigital electrode topology have pronounced persistent conductivity. It is shown that the magnitude of responsivity, response time  $\tau_r$ , and recovery time  $\tau_d$  are determined by the concentration of free holes  $p$  involved in recombination processes. For the first time, it is proposed to consider hole trapping both by surface states  $N_{ts}$  at the metal/Ga<sub>2</sub>O<sub>3</sub> interface and by traps in the bulk of the film.

**Keywords:** gallium oxide; MSM structures; UV radiation; traps; persistent conductivity; RFMS



**Citation:** Kalygina, V.M.; Tsymbalov, A.V.; Korusenko, P.M.; Koroleva, A.V.; Zhizhin, E.V. Effect of Traps on the UV Sensitivity of Gallium Oxide-Based Structures. *Crystals* **2024**, *14*, 268. <https://doi.org/10.3390/cryst14030268>

Academic Editors: Andrew F. Zhou and Peter X. Feng

Received: 8 February 2024

Revised: 27 February 2024

Accepted: 6 March 2024

Published: 9 March 2024



**Copyright:** © 2024 by the authors. Licensee MDPI, Basel, Switzerland. This article is an open access article distributed under the terms and conditions of the Creative Commons Attribution (CC BY) license (<https://creativecommons.org/licenses/by/4.0/>).

## 1. Introduction

In recent years, the exploration of advanced materials for electronic devices has led to the emergence of gallium oxide (Ga<sub>2</sub>O<sub>3</sub>) as a promising semiconductor for various applications, particularly in the development of detectors [1,2]. Gallium oxide, a wide-bandgap semiconductor ( $E_g = 4.4\text{--}5.3$  eV), exhibits unique properties that make it well suited for high-performance ultraviolet sensors [3,4]. This compound has attracted considerable attention in the field of optoelectronics due to its wide bandgap energy, excellent thermal stability, and robust chemical properties [5,6]. Ultraviolet detectors (UVDs) based on gallium oxide have found a wide range of applications in areas such as environmental monitoring, flame detection, communication systems, biomedical applications, etc. [7,8].

The sensitivity of UVDs to UV radiation and their speed of operation are the main parameters characterizing their ability to detect UV radiation and the time resolution of the devices, respectively [9]. Previous works have demonstrated detectors based on Ga<sub>2</sub>O<sub>3</sub> with high values of responsivity ( $R$ ), detectivity ( $D^*$ ), and external quantum efficiency (EQE) [10]. However, response times  $\tau_r$  and recovery times  $\tau_d$  exceeded several seconds. In this regard, the development of ultraviolet detectors with minimal response  $\tau_r$  and recovery times  $\tau_d$  as well as high sensitivity is an important task.

In  $\beta$ -Ga<sub>2</sub>O<sub>3</sub>, there are many deep traps in the bandgap, formed by structural defects and impurities [11]. Deep traps in  $\beta$ -Ga<sub>2</sub>O<sub>3</sub> can be classified into two types: majority and minority traps. This classification is either based on their capability to capture an electron (majority trap) or a hole (minority trap), which is clearly manifested in the capture cross-section rate value, or depends on how close they are to the valence band maximum and conduction band minimum [12].

Recent research on deep electron traps in n-type  $\beta$ -Ga<sub>2</sub>O<sub>3</sub> Schottky barrier diodes (SBDs) has enabled the mapping of the upper half of the bandgap and revealed the presence of four deep electron traps with activation energy values near  $E_c - 0.6$  eV (E1),  $E_c - 0.79$  eV (E2),  $E_c - 0.75$  eV (E2\*), and  $E_c - 1$  eV (E3) [12].

Ga<sub>2</sub>O<sub>3</sub>-based UVDs exhibit persistent conductivity [13]. This is due to holes that can self-localize on defects in the gallium oxide crystal lattice [14]. As a result, the response and recovery times of gallium oxide UVDs can be several minutes. Minority traps H1, H2, and H3, with energies of about 0.2, 0.3, and 1.3 eV, respectively, above the valence band maximum are the most known defects that are related to gallium vacancy [12]. Therefore, the study of the effect of traps on photoelectric performance plays a key role in the development and optimization of gallium oxide detectors [15].

This work considers ultraviolet radiation detectors based on M/ $\beta$ -Ga<sub>2</sub>O<sub>3</sub>/M with different interelectrode distances and topologies. The responsivity values of the structures were compared with their response  $\tau_r$  and recovery times  $\tau_d$ . An analysis of their current–voltage characteristics (I–V characteristics) was carried out over a wide voltage range. For the first time, it was proposed to take into account surface states at the gallium oxide/metal interface which are involved in the capture of free holes.

## 2. Experimental Procedure

### 2.1. Methodology of Structure Production

In this work, two types of detectors based on  $\beta$ -Ga<sub>2</sub>O<sub>3</sub> were studied: detectors with two parallel electrodes (the first sample type) and detectors with interdigitated electrodes (the second sample type).

Electrodes for detectors of the first type were created by depositing a layer of platinum on smooth sapphire substrates using the vacuum deposition method. In the next stage, contacts were formed using explosive photolithography. The distance between the electrodes was 250  $\mu$ m (Figure 1a). A gallium oxide film 150–200 nm thick was deposited by radio-frequency magnetron sputtering (RFMS) of a Ga<sub>2</sub>O<sub>3</sub> target (99.999%) onto unheated sapphire substrates using an AUTO-500 setup (Edwards, UK) in an Ar/O<sub>2</sub> gas mixture. The oxygen concentration in the mixture was  $(56.1 \pm 0.5)$  vol. %. The distance between the target and the substrate was 70 mm. The pressure in the chamber during spraying was maintained at  $7 \times 10^{-6}$  bar. Then, the gallium oxide film was annealed in argon at 900 °C for 30 min. After annealing, the film transformed from an amorphous state to a polycrystalline beta phase of Ga<sub>2</sub>O<sub>3</sub> [16]. The wafer was then cut into  $1.4 \times 1.4$  mm<sup>2</sup> chips, as shown in Figure 1a.

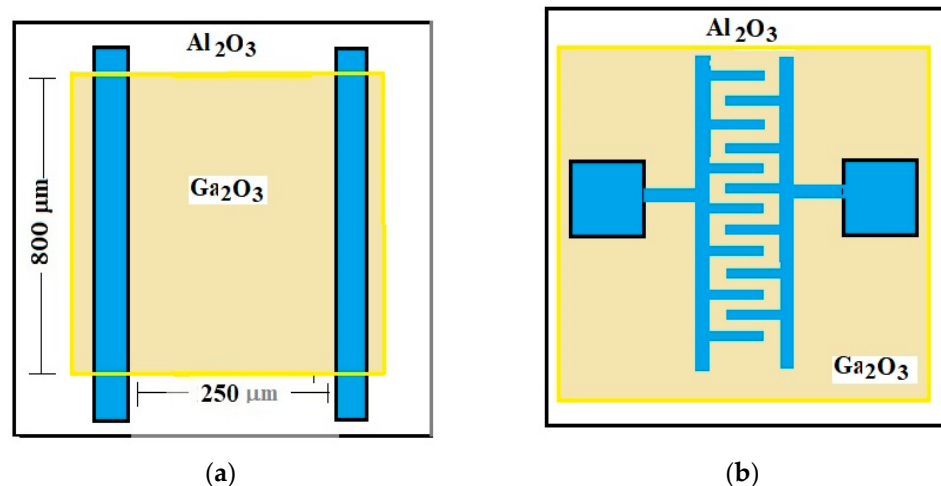


**Figure 1.** Schematic representation of detectors with two parallel electrodes (a) and detectors with interdigitated electrodes (b).

The second type of detectors was prepared similarly, with the exception that a gallium oxide film was first deposited onto a sapphire substrate. Following this, an interdigitated topology of Ti/V-based electrodes was formed. Samples with interelectrode distance  $d$  equal to 50, 30, 10, and 5  $\mu\text{m}$  were obtained. The number of electrodes was 50, 75, 150, and 200, respectively. The chips were  $3.5 \times 3.5 \text{ mm}^2$  in size, regardless of interelectrode distance (Figure 1b).

## 2.2. Structural Property Characterization and Electrical Measurements

X-ray diffraction (XRD) spectra of  $\text{Ga}_2\text{O}_3$  films before and after annealing were measured by a Bruker D8 Discover (Bruker AXS GmbH, Germany) diffractometer (CuK  $\alpha$  radiation  $\lambda = 1.54 \text{ \AA}$ ) with a position-sensitive linear detector LynxEye in Bragg–Brentano geometry at an  $\omega = 0.5^\circ$  angle offset from the normal position of the sapphire substrate.

The chemical composition of the samples was studied by X-ray photoelectron spectroscopy (XPS). XPS measurements were carried out using a hemispherical analyzer included in the ESCALAB 250Xi (Thermo Fisher Scientific, Waltham, MA, USA) laboratory spectrometer. The measurements were carried out using a monochromatized AlK $\alpha$  radiation ( $h\nu = 1486.6 \text{ eV}$ ). Survey and core-level (Ga 2p, O 1s, Ga 3d) photoemission (PE) spectra were recorded in the constant-energy mode of the analyzer with pass energies of 100 and 50 eV, respectively. The film's surface was irradiated with argon ions at an average energy of 500 eV for 300 s to remove adsorbed atoms and molecules of contaminants. The analysis of the core-level spectra was processed using Avantage Data System software.

The spectral dependencies of the photoelectric properties were measured by means of the spectrometric system based on a MonoScan 2000 monochromator (Ocean Insight, Orlando, FL, USA) and a DH-2000 Micropack lamp, described in detail in [10]. A krypton-fluorine lamp VL-6.C was used as the source of irradiation at  $\lambda = 254 \text{ nm}$  and the light power density  $P = 780 \mu\text{W}/\text{cm}^2$ . The photoelectric and electrical properties of the samples were measured by means of Keithley 2611B.

## 3. Results

Figure 2 shows the XRD spectra of the gallium oxide film before and after annealing at  $900^\circ\text{C}$ . Peaks at  $2\theta = 41.7^\circ$  and  $90.7^\circ$  correspond to (0006) and (00012) crystals planes of sapphire substrates. The gallium oxide thin film without annealing is amorphous (Figure 2, black line). The film annealed at  $900^\circ\text{C}$  has peaks of the monoclinic  $\beta\text{-Ga}_2\text{O}_3$  phase (Figure 2, red line and blue bars). A partial texture with a preferred orientation of (20-1)  $\text{Ga}_2\text{O}_3$  planes parallel to the substrate surface is formed in the annealed film.

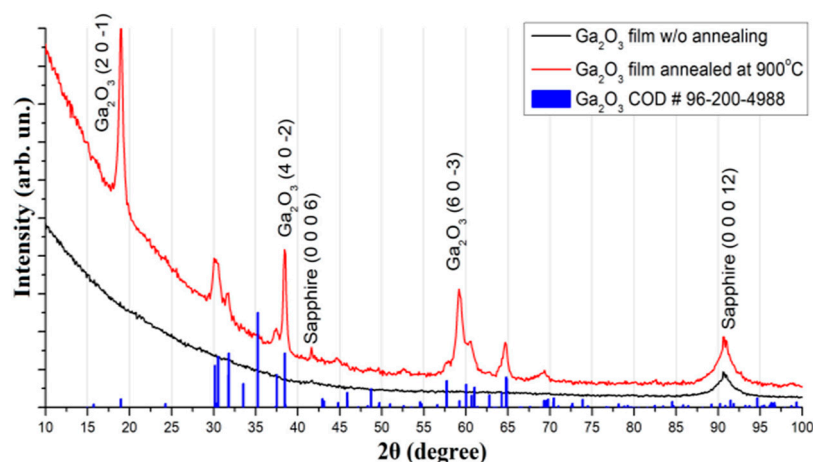
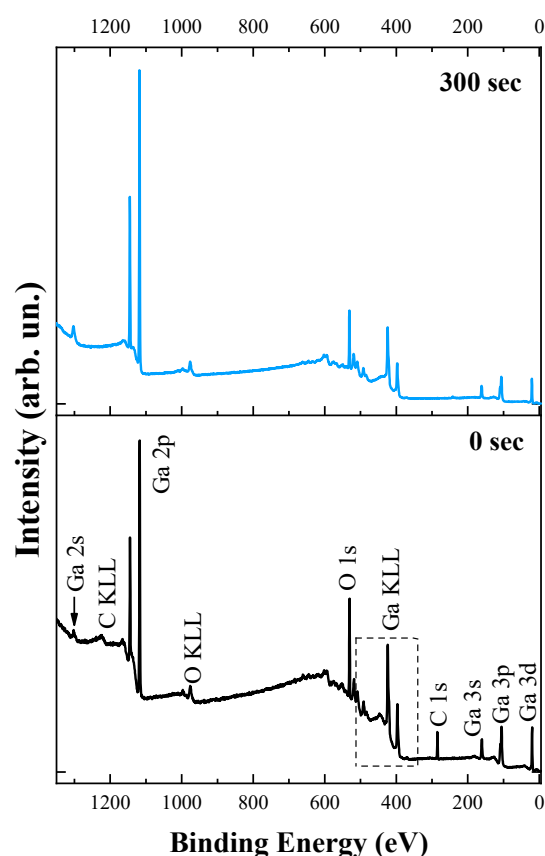


Figure 2. XRD pattern of gallium oxide film without annealing and annealed at  $900^\circ\text{C}$ .

Figure 3 shows the survey spectra of the studied sample before and after 300 s etching with argon ions. In both survey PE spectra, gallium (Ga 2s~1303 eV, Ga 2p~1118.1 eV, Ga LMM~424.5 eV, Ga 3s~161.2 eV, Ga 3p~106.1 eV, and Ga 3d~20.8 eV) and oxygen lines

(O KLL~976.5 eV, O 1s~531.4 eV, O 2s~24 eV) are present [17]. At the same time, the survey spectrum measured from the surface before etching also contains carbon lines (C KLL~1224 eV, C 1s~285 eV). After etching with argon ions, the intensity of the O 1s PE line decreases significantly, and the intensity of the Ga 2p PE line, on the contrary, increases. This result indicates a change in the [O]/[Ga] ratio. It is important to note that for a more correct quantitative analysis and determination of the [O]/[Ga] ratio, the gallium Ga 3s and the oxygen O 1s lines were used. This is due to the fact that the escape depths of photoelectrons, which are determined by the inelastic mean free path (IMFP) of a photoelectron, for these shells are ~2.2 and ~1.7 nm, respectively, while for the Ga 2p and O 1s shells, the IMFP differs by almost 2 times (see Table 1). It is clearly seen that the [O]/[Ga] ratio differs before and after ion etching; the reasons for this are outlined in the Discussion section.



**Figure 3.** Survey PE spectra of the RFMS-deposited  $\beta$ -Ga<sub>2</sub>O<sub>3</sub> film, measured before and after 300 s etching with argon ions.

**Table 1.** Elemental composition of the RFMS-deposited  $\beta$ -Ga<sub>2</sub>O<sub>3</sub> film.

Ga <sub>2</sub> O <sub>3</sub> Film	Concentration, at. %		IMFP *, nm				[O]/[Ga]	
	[O] O 1s	[Ga] Ga 3s	Ga 2p	O 1s	Ga 3s	Ga 3p		Ga 3d
Surface (no etching)	59.80	40.20	0.88	1.72	2.21	2.28	2.39	1.48
After 300 s Ar <sup>+</sup> etching	54.4	45.6						1.19

\* IMFP—inelastic mean free path.

A detailed analysis of the core-level PE spectra measured after 300 s Ar<sup>+</sup> etching showed that the positions of the Ga 2p<sub>3/2</sub>, Ga 3d, and O 1s line maxima at the binding energy are 1118.1, 20.6, and 531.1 eV, respectively. This result, together with the [O]/[Ga] ratio, indicates that gallium is in the Ga<sub>2</sub>O<sub>3</sub> compound (Figure 4) [18].

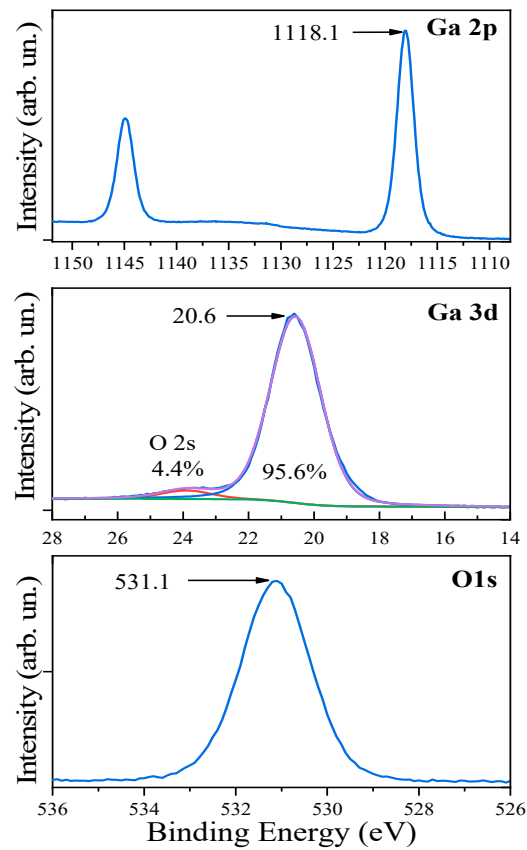


**Figure 4.** Ga 2p, Ga 3d, and O 1s PE spectra of the RFMS-deposited  $\beta$ -Ga<sub>2</sub>O<sub>3</sub> film, measured after 300 s etching with argon ions.

Figure 5 shows the transmission spectrum for  $\beta$ -Ga<sub>2</sub>O<sub>3</sub> films. Gallium oxide films are transparent in the near-ultraviolet (UVA) range. The transmittance values  $T$  decrease from 83% to 74.5% between wavelengths of 320 nm and 280 nm. The structures are solar-blind. The optical bandgap of the  $\beta$ -Ga<sub>2</sub>O<sub>3</sub> film was determined by analyzing the dependence of the absorption coefficient  $\alpha$  on photon energy  $h\nu$ , resulting in  $E_g = 4.8 \pm 0.05$  eV (Figure 5, inset).

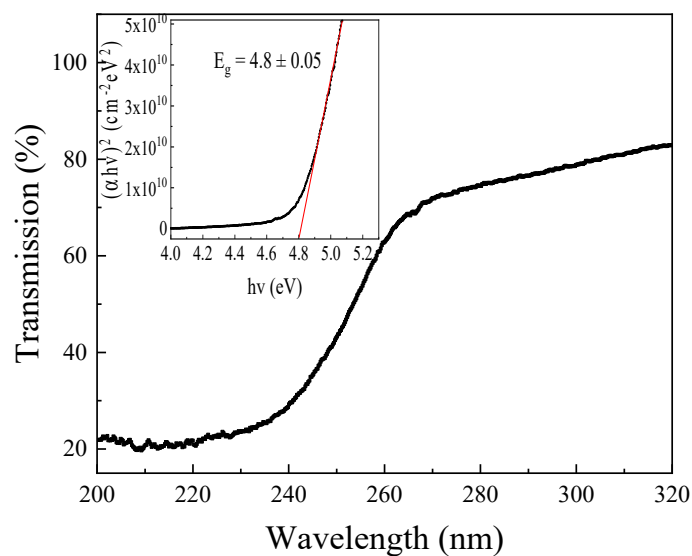


**Figure 5.** Transmission spectrum of the RFMS-deposited  $\beta$ -Ga<sub>2</sub>O<sub>3</sub> films. Dependence of  $\alpha^2$  on photons energy (black curve) is shown in insertion (red curve—approximation of the linear section).

### 3.1. Structures of the First Type

The current–voltage characteristics of both sample types are symmetrical regarding voltage polarity. The dependence of the dark current ( $I_D$ ) on the voltage ( $U$ ) is linear for detectors of the first type.  $I_D$  values do not exceed 10–180 pA in the voltage range  $-200 \leq U \leq 200$  V (Figure 6a). The current–voltage characteristic maintains a linear shape under UV exposure (Figure 6b). Ultraviolet radiation with a wavelength of 254 nm leads to an increase in current by 3–4 orders of magnitude. Total current ( $I_L$ ) values increase linearly under UV exposure to 1.6–1.7  $\mu$ A with increasing voltage up to  $\pm 200$  V. In Figure 6, the  $I_{L1}$  and  $I_{L2}$  curves correspond to the currents measured during the first and second measurements of the structures during continuous exposure to UV radiation.

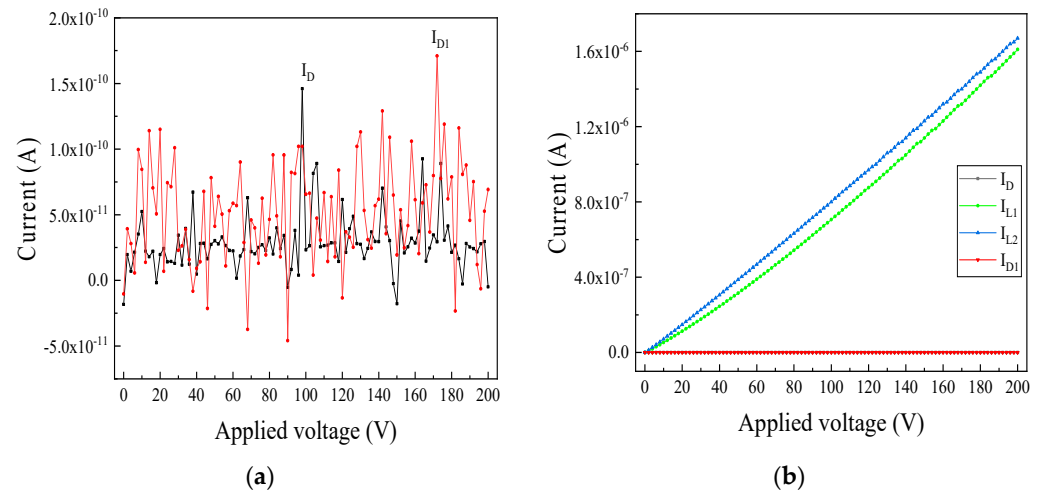


**Figure 6.** Dark current–voltage characteristics (a) and current–voltage characteristics measured under exposure to radiation with  $\lambda = 254$  nm (b).  $I_D$  and  $I_{D1}$  are dark currents measured before ( $I_D$ ) and immediately after turning off the UV radiation ( $I_{D1}$ );  $I_{L1}$  and  $I_{L2}$  are currents measured during exposure to radiation with  $\lambda = 254$  nm.

Figure 6a shows that the dark current  $I_{D1}$  returns to its original values  $I_D$  almost immediately after exposure to UV radiation. The dark currents measured before and immediately after turning off the UV light are consistent within experimental error (Figure 6a). Thus, the structures do not exhibit “persistent conductivity”.

Figure 7 shows the time profile of the current structure under UV exposure with  $\lambda = 254$  nm. The response times  $\tau_r$  and recovery times  $\tau_d$  of the photocurrent are in the millisecond range, confirming the absence of “persistent conductivity” in samples of this type.

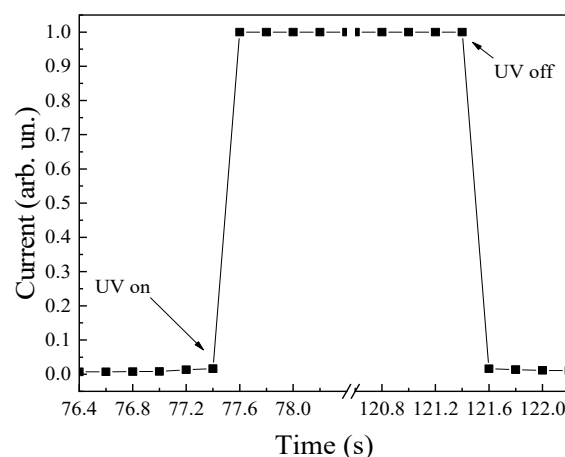


**Figure 7.** Time dependence of the normalized  $I_L$  at  $\lambda = 254$  nm,  $P = 780 \mu\text{W}/\text{cm}^2$ , and  $U = 1$  V.

### 3.2. Structures of the Second Type

The current–voltage characteristics of structures with interdigitated contacts (structures of the second type) and interelectrode distances of 50 and 30  $\mu\text{m}$  are linear in the range of 0 to 200 V (Figure 8).

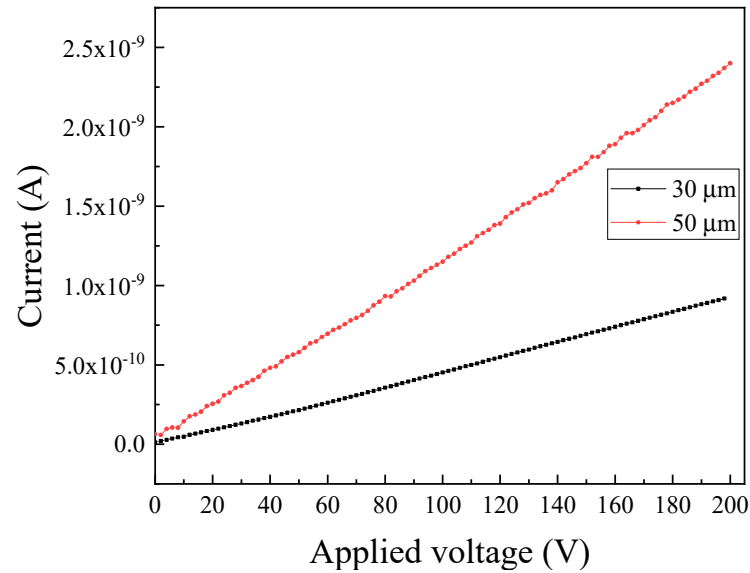


**Figure 8.** Dark current–voltage characteristics of samples with interdigitated electrodes and interelectrode distances of 50  $\mu\text{m}$  (red curve) and 30  $\mu\text{m}$  (black curve).

The dark I–V shape changes as the interelectrode distance decreases in structures with interdigitated electrodes. Thus, the dark current–voltage characteristics of the samples with an interelectrode distance of 5  $\mu\text{m}$  and 10  $\mu\text{m}$  cannot be represented by a linear dependence of current  $I$  on voltage  $U$  in the range of the indicated voltages (Figure 9, inset). Figure 9 shows the dark current–voltage characteristics on a double logarithmic scale for samples with an interelectrode distance of 5  $\mu\text{m}$  and 10  $\mu\text{m}$  in the voltage range  $0 < V \leq 200$  V.

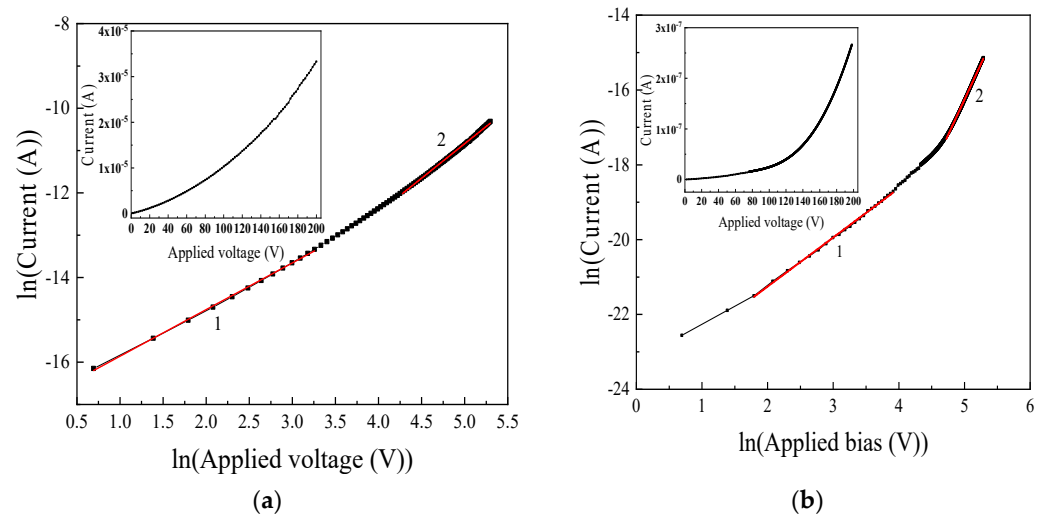


**Figure 9.** Dark current–voltage characteristics of samples with interdigitated electrodes and interelectrode distances of 5  $\mu\text{m}$  (a) and 10 (b)  $\mu\text{m}$  on a double logarithmic scale (insert current–voltage curve in linear coordinates).

The coordinates  $\ln(I)$  from  $\ln(U)$  contain linear sections. The slope of the first section is 1.10 for the structure with an interelectrode distance of 5  $\mu\text{m}$  and 1.63 for the second section. For a structure with an interelectrode distance of 10  $\mu\text{m}$ , the slope of the first

section is 1.31, and for the second—3.80. Thus, the dark current–voltage characteristics of samples with interelectrode distances  $d = 5$  and  $10 \mu\text{m}$  can be represented by power law dependence  $I \sim U^m$ , where  $m = 1$  in the range of low voltages and  $m > 1$  at higher electric fields. Thus, the conductivity of structures of the second type in the absence of radiation is determined by space-charge-limited currents (SCLCs) in a semiconductor with traps unevenly distributed in energy (Figure 9). The relationship between current and voltage in this case is determined by the following expression [19]:

$$J = N_c \mu e^{1-l} \left[ \frac{\varepsilon \varepsilon_0 l}{N_t (l+1)} \right]^l \left( \frac{2l+1}{l+1} \right)^{l+1} \frac{U^{l+1}}{d^{2l+1}} \quad (1)$$

where  $N_c$  is the effective density of quantum states in the conduction band of gallium oxide;  $\varepsilon$ —the relative permittivity of  $\text{Ga}_2\text{O}_3$ ;  $\varepsilon_0$ —the electrical constant;  $\mu$ —electron mobility;  $N_t$  is the concentration of traps in the  $\text{Ga}_2\text{O}_3$  film;  $e$ —electron charge;  $l = m - 1$ . Exponent  $l$  was determined from the slope of the current–voltage characteristic on a double logarithmic scale. The transition voltage from Ohm’s law to SCLC is described by the following expression:

$$U_{\Omega \rightarrow T} = \frac{ed^2}{\varepsilon \varepsilon_0} \left( \frac{l+1}{2l+1} \right)^{(1+l)/l} N_t \left( \frac{n_0}{N_c} \right)^{1/l} \left( \frac{l+1}{l} \right). \quad (2)$$

From experimental data and Expression (2), it was found that the trap concentration  $N_t$  was  $2 \times 10^{17} \text{ cm}^{-3}$  and  $6 \times 10^{17} \text{ cm}^{-3}$  for structures with  $d = 5$  and  $10 \mu\text{m}$ , respectively. The value of  $N_t$  was calculated using  $n_0 = 1 \times 10^{17} \text{ cm}^{-3}$  and  $N_c = 4 \times 10^{18} \text{ cm}^{-3}$  [20]. The conclusion regarding SCLCs in these samples is consistent with the established concept of multiple traps in the bandgap of  $\beta\text{-Ga}_2\text{O}_3$  [21–23].

In structures with interdigitated electrodes (structures of the second type), the dependence of current  $I_L$  on voltage cannot be represented by a linear dependence, regardless of the interelectrode distance (Figure 10a).

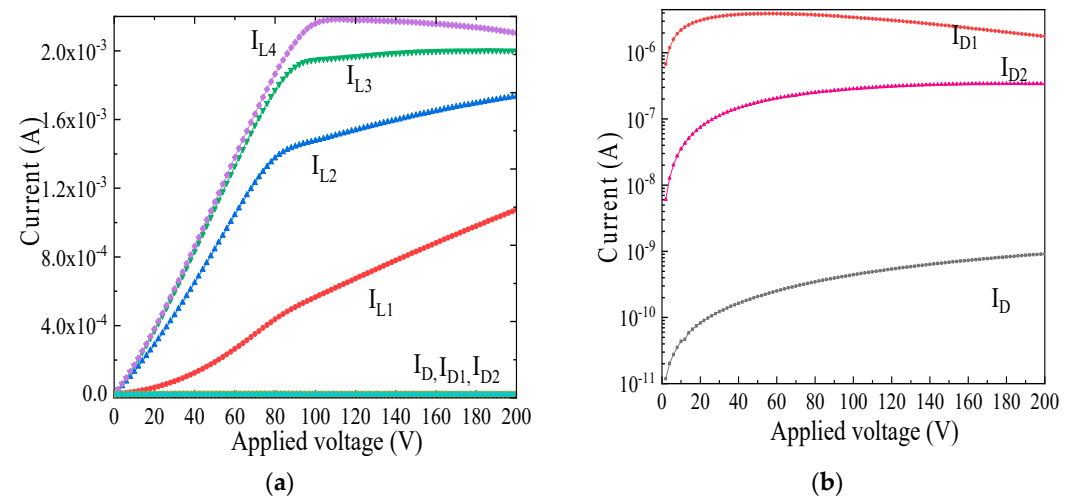


**Figure 10.** Current–voltage characteristics of the second sample type with  $d = 30 \mu\text{m}$ . (a):  $I_{L1}$ – $I_{L4}$ —currents measured during exposure to radiation with  $\lambda = 254 \text{ nm}$ ; (b):  $I_D$ —initial dark current,  $I_{D1}$ —dark current measured immediately after UV exposure,  $I_{D2}$ —dark current measured immediately after  $I_{D1}$ .

Initially,  $I_L$  increases linearly with increasing voltage, and then a slowdown in the growth of the light current is observed, followed by a decrease, for example, in the  $I_{L4}$  curve in Figure 10a.

The light current increases with each subsequent measurement:  $I_{L1} < I_{L2} < I_{L3} < I_{L4}$  during continuous exposure to radiation with  $\lambda = 254 \text{ nm}$  (Figure 10a). Further measurements lead to the stabilization of the light current: it reaches a stationary state.

A similar behavior of the current–voltage characteristic under continuous UV exposure is typical for samples with  $d = 10 \mu\text{m}$  (Figure 11a). In the region of strong electric fields, a noticeable decrease in light current is observed with increasing voltage in the structure (Figure 11a, curves  $I_{L1}$ – $I_{L8}$ ). The maximum points of  $I_L$  from  $U$  were determined by differentiation (Figure 11b).

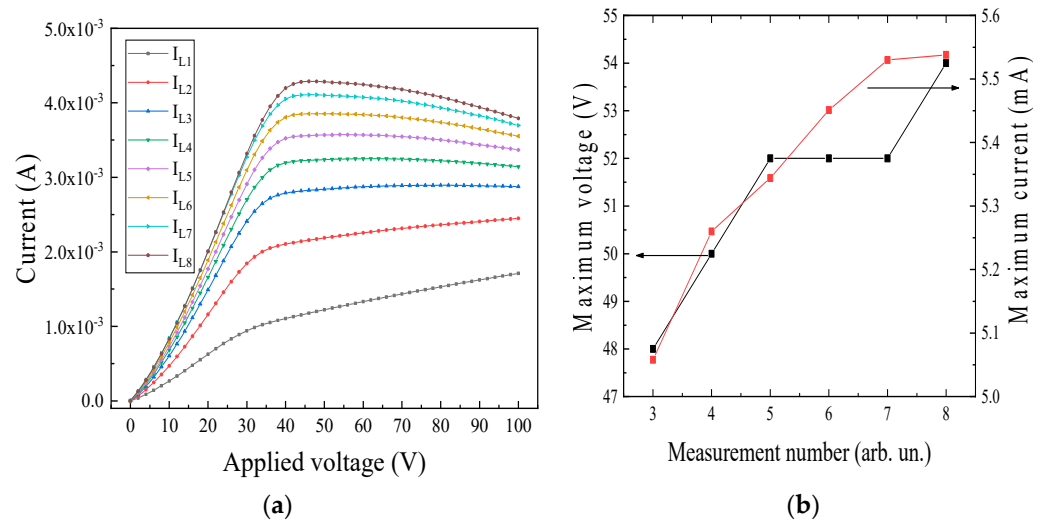


**Figure 11.** I–V characteristics of the second type of sample with  $d = 10 \mu\text{m}$ . (a)  $I_{L1}$ – $I_{L8}$  currents measured during exposure to radiation with  $\lambda = 254 \text{ nm}$ ; (b) dependence of the maximum current value and the corresponding voltage on the measurement number.

It should be noted that the behavior of the current–voltage characteristic is also affected by radiation with energy  $h\nu < E_g$ . In [16], the influence of pre-exposure of the structure to radiation with quanta of energy  $h\nu$  less than the bandgap  $E_g$  of gallium oxide on the behavior of the current–voltage characteristic is considered. Pre-exposure to broadband radiation increases the photocurrent  $I_{L1}$  generated by short-wavelength radiation and reduces the deviation of photocurrents  $I_{L2}$ ,  $I_{L3}$ , and  $I_{L4}$  from  $I_{L1}$  (first measurement) (Figure 12).

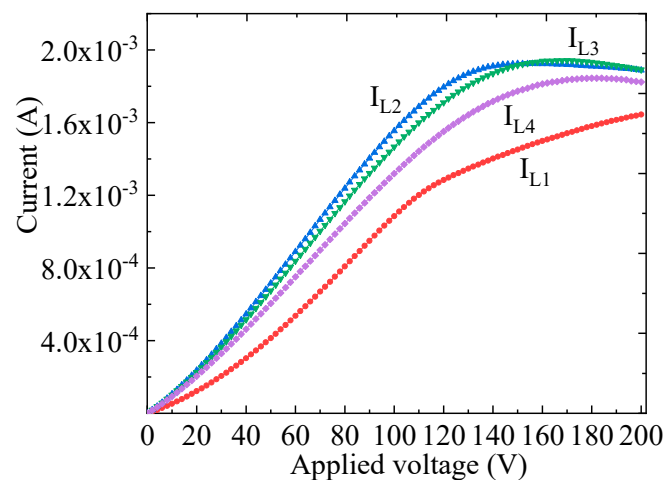


**Figure 12.** Current–voltage characteristics of a sample with  $d = 30 \mu\text{m}$  after exposure to broadband radiation with  $h\nu < E_g$ ; the designations are the same as in Figure 10.

Exposure to radiation with  $h\nu < E_g$  reduces the concentration of active trap centers due to changes in their charge state. This leads to an increase in the photocurrent and stability of detectors in the UV range [16].

Dark current  $I_D$  takes some time to return to its initial value after exposure to UV radiation. In other words, the samples have persistent photoconductivity. Figure 10b shows

dark current–voltage characteristics measured at different times: before UV exposure ( $I_D$ ); after UV exposure ( $I_{D1}$ ); and 30 s after UV exposure ( $I_{D2}$ ). The dark current measured immediately after turning off the UV is 3–4 orders of magnitude higher than the initial values of dark current  $I_D$  at sample voltages  $0 \leq U \leq 200$  V. The presence of a maximum in the  $I_{D1}$  curve is explained by the gradual relaxation of the residual current as the voltage across the structure increases.

Thus, characteristics of structures with interdigitated electrodes are a large responsivity value and the presence of “persistent conductivity”. Table 2 shows the responsivity  $R$  and detectivity  $D^*$  values for structures of the first and second types. The responsivity and detectivity values were calculated using the following expressions [24]:

$$R = \frac{I_L - I_D}{P_s}, \quad (3)$$

$$D^* = R \sqrt{\frac{s}{2eI_D}} \quad (4)$$

where  $P$ —light power density,  $s$ —effective area,  $e$ —electron charge [7].

**Table 2.** Photoelectric characteristics of structures with different interelectrode distances under UV irradiation,  $\lambda = 254$  nm.

$d, \mu\text{m}$	$s, \text{cm}^2$	$I_D, \text{A}$	$I_L, \text{A}$	$R, \text{A/W}$	$D^*, \text{Jones}$	$\text{Bias, V}$
5	0.0125	$1.96 \times 10^{-10}$	$7.5 \times 10^{-3}$	770	$1.1 \times 10^{16}$	30
10	0.0174	$1.01 \times 10^{-10}$	$4.7 \times 10^{-3}$	350	$8.1 \times 10^{15}$	30
30	0.0247	$1.20 \times 10^{-9}$	$2.1 \times 10^{-3}$	110	$8.8 \times 10^{14}$	200
50	0.0270	$2.77 \times 10^{-9}$	$1.0 \times 10^{-3}$	47	$2.6 \times 10^{14}$	200
250	0.0020	$4.30 \times 10^{-11}$	$1.6 \times 10^{-6}$	1.0	$1.2 \times 10^{13}$	200

#### 4. Discussions

Based on the XRD and XPS spectra, as well as the dependence of the absorption coefficient  $\alpha$  on energy  $h\nu$ , it can be concluded that the film deposited using the RFMS method is  $\beta\text{-Ga}_2\text{O}_3$ . However, in the XPS data, a significant decrease in the  $[\text{O}]/[\text{Ga}]$  ratio from 1.48 to 1.19 was found after ion beam etching (see Table 1). This result is not associated with the presence of an oxygen-depleted layer in the  $\text{Ga}_2\text{O}_3$  film but is explained by the removal of oxygen atoms from the  $\text{Ga}_2\text{O}_3$  crystal lattice under the influence of argon ions during long-term treatment of the film surface. This effect was previously observed during the etching of various metal oxides with argon ions, as presented in [25]. Thus, the film obtained in this work is represented by stoichiometric  $\text{Ga}_2\text{O}_3$  with a low content of oxygen vacancies.

Figure 13 shows the energy diagram of the  $\text{M}/\text{Ga}_2\text{O}_3/\text{M}$  structure. The energy diagram shown takes into account the ratios of the work function of electrons from metals  $\chi_0$  used in our experiments (4.3 eV—Ti, V and 5.7 eV—Pt), and the electron affinity of  $\text{Ga}_2\text{O}_3$  (4.0 eV) [26,27].

The conductivity of structures for both types in the absence of radiation is determined by space-charge-limited currents (SCLCs) in a trap semiconductor. The transition voltage from Ohm’s law to the power law dependence of current on voltage depends on the concentration of traps in the oxide film  $N_t$  and is proportional to  $d^2$ , as follows from Expression (2). Transition voltage increases with the increasing concentration of free traps (those that have not captured electrons). It is assumed that in structures of the first type with two parallel electrodes, the concentration of free traps is high. Therefore, it is not possible to achieve a transition voltage in the voltage range  $0 \leq U \leq 200$  V. The high concentration of free traps causes low responsivity values  $R$  (Table 2) and relatively short response and recovery times.

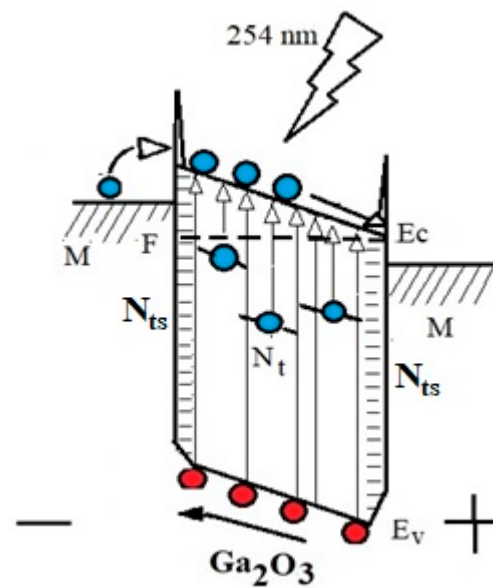


**Figure 13.** Schematic representation of the energy diagram of M/Ga<sub>2</sub>O<sub>3</sub>/M.

It is assumed that structures with interdigitated electrodes have a higher density of surface states ( $N_{ts}$ ) at the M/Ga<sub>2</sub>O<sub>3</sub> interface, which are divided into fast and slow. The average energy density of surface states should be the same for all samples obtained in one technological cycle. Then, the total number of  $N_{ts}$  is determined by the contact perimeter  $W$ . The  $W$  values for the studied samples depend on the topology of the contacts and are given in Table 3. States above the Fermi level are able to trap holes at negative potentials on contact (Figure 13). Trapped holes do not contribute to recombination. As a result, a high concentration of generated electrons remains in the conduction band, which explains the large responsivity values presented in Table 3. In addition, the accumulation of holes on the negative electrode leads to the formation of an internal field.

**Table 3.** Time characteristics of structures under UV exposure with  $\lambda = 254$  nm as a function of electrode perimeter.

$d, \mu\text{m}$	$W, \text{cm}$	$\tau_{r1}, \text{s}$	$\tau_{r2}, \text{s}$	$\tau_{d1}, \text{s}$	$\tau_{d2}, \text{s}$
5	39.8	0.63	15.5	0.02	2.12
50	9.95	0.28	14.5	0.05	2.30
250	0.16	0.07	1.72	0.051	0.53

Figures 10a and 11a demonstrate the significant impact of traps on the response magnitude. The  $I_L$  value increases until it reaches a steady-state value with each subsequent measurement. The current–voltage characteristic's behavior is due to the gradual filling of traps. These traps capture electrons and do not participate in recombination processes during subsequent measurements.

The structures with interdigitated electrodes exhibit a monotonic dependence of current on voltage in the first measurement. However, the shape of the dependence of  $I_L$  on  $U$  changes with subsequent measurements (Figures 10a and 11a). Deviation from the monotonic dependence of light current on voltage occurs at electric fields above a certain critical value  $E_{cr}$  [28]. The critical field is defined as the electric field strength at which the drift length  $L_E$  is equal to twice the hole diffusion length ( $L_E = 2L_p$ ) [29].

As the voltage increases,  $I_L$  becomes dependent on voltage in the form of a curve with a maximum. The decrease in  $I_L$  at voltages exceeding  $V_{max}$  is due to the appearance of an internal electric field  $E_{in}$ , in the opposite direction of the external field  $E_{ex}$ . The voltage  $V_{max}$ , corresponding to the maximum value of the light current, increases with subsequent measurements (Figure 11b). The effect is explained by an increase in internal field strength

$E_{in}$  with increasing photocurrent, and higher values of  $E_{ex}$  are required to compensate for it. It should be noted that the internal electric field plays a significant role at values of  $I_L = 10^{-4}$ – $10^{-3}$  A.

The time dependences of  $I_L(t)$  are characterized by two processes: fast and slow changes in current. The fast stage of change in  $I_L$  is determined by processes of generation of electrons from the valence band and excitation of electrons from trap centers located below the Fermi level into the conduction band. The capture of electrons and holes at trap centers occurs simultaneously with the generation process.

Slow processes are caused by recombination (mainly Shockley–Reed–Hall recombination) and capture by traps. The recombination rate  $\Delta n/\tau_n$  depends on the concentration of free holes in the valence band. An increase in the concentration of free holes in the valence band increases the rate of recombination. Thus, the stationary state is established faster, determined by the radiation intensity and the voltage on the structure. In turn, trapped  $p_t$  holes do not participate in recombination. An increase in  $p_t$  leads to a decrease in the recombination rate and an increase in the response times  $\tau_r$  and recovery times  $\tau_d$ . Thus, trapped holes cause high photocurrent values.

It is assumed that free holes are captured not only by defects in the bulk of the gallium oxide film, but also by surface states at the metal/ $\text{Ga}_2\text{O}_3$  interface. Table 3 shows the response and recovery times for structures with different interelectrode distances. The P parameter determines the perimeter of the contacts used. Times  $\tau_r$  and  $\tau_d$  were found as the average value measured for each of the pulses shown in Figure 14.

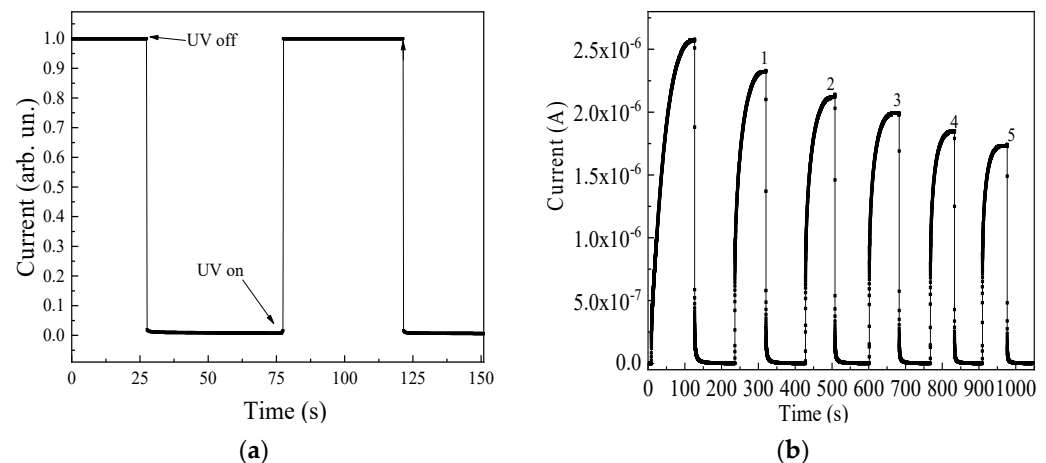


**Figure 14.** Time dependence of  $I_L$  for structures with two electrodes (a) and with interdigitated electrodes  $d = 50 \mu\text{m}$  (b) under UV exposure with  $\lambda = 254 \text{ nm}$  and applied bias  $U = 1 \text{ V}$ .

From Table 3 and Figure 14, we can draw the following conclusions:

1. The response  $\tau_r$  and recovery times  $\tau_d$  of the photocurrent in structures with interdigitated electrodes are described by the following expression [30]:

$$I = I_s + A \times \exp(-t/\tau_{r1}) + B \times \exp(-t/\tau_{r2}), \quad (5)$$

$$I = I_s + A \times \exp(-t/\tau_{d1}) + B \times \exp(-t/\tau_{d2}), \quad (6)$$

where  $I_s$  represents the steady-state current and  $A$  and  $B$  are the fitting constants.  $\tau_{r1}$  and  $\tau_{r2}$  are fast and slow components of response times, whereas  $\tau_{d1}$  and  $\tau_{d2}$  denote the fast and slow components of recovery times;

2. Structures with interdigitated electrodes have recovery times that are an order of magnitude shorter than their response times;
3. The maximum value of  $I_L$  decreases with each successive UV exposure (Figure 14b);
4. The minimum values of  $\tau_r$  and  $\tau_d$  correspond to structures with two electrodes, which have the lowest responsivity (Table 3).

The differences in responsivity values and time parameters between structures of the first and second types are explained by the different concentrations of traps that take part in the processes of generation and recombination.

Considering the metal/Ga<sub>2</sub>O<sub>3</sub> interface, it is important to take into account the surface states, whose number depends on the perimeter of the contacts  $W$ . The Table 3 shows that the lowest  $W$  values were obtained for two-electrode samples. At a low concentration of surface states, a large fraction of the generated holes remain free and are capable of participating in recombination. Thus, there is a low concentration of electrons remaining in the conduction band. Consequently, the response values  $R$  (Table 2) are relatively small, and the values of  $\tau_r$  and  $\tau_d$  are fast (Table 3, Figure 14a).

Structures with large  $W$  values ( $d = 5 \mu\text{m}$ ) exhibit maximum responsivity  $R$  and the longest  $\tau_r$  and  $\tau_d$  times (Tables 2 and 3). Increasing the interelectrode distance to  $50 \mu\text{m}$  leads to a fourfold decrease in  $W$ . As a result, responsivity is reduced by one order of magnitude, and recovery times are cut in half.

Studies of isotopic and anisotypic Ga<sub>2</sub>O<sub>3</sub> semiconductor heterostructures confirm the crucial role of free holes in responding to far-range UV radiation [31,32]. The presence of a source of free holes in the valence band of the semiconductor provides a high recombination rate and low values of  $\tau_r$  compared to similar data for samples with interdigitated electrodes.

## 5. Conclusions

The electrical and photoelectric characteristics of thin-film M/Ga<sub>2</sub>O<sub>3</sub>/M structures with two parallel electrodes ( $d = 250 \mu\text{m}$ ) and interdigitated contacts with interelectrode distances  $d = 50, 30, 10,$  and  $5 \mu\text{m}$  were studied.

The dark currents of the studied structures, regardless of interelectrode distance, were caused by currents limited by the space charge in the semiconductor. Traps were exponentially distributed in the bandgap of gallium oxide. The concentration of trap centers, estimated from experimental data, was  $(4\text{--}6) \cdot 10^{17} \text{cm}^{-3}$ .

The relationship between the magnitude of responsivity and the time characteristics for structures with different electrode topologies was considered. It was shown that the response and time parameters  $\tau_r$  and  $\tau_d$  are determined by the concentration of free holes  $p$  participating in recombination processes. However, the presence of free holes depends on the concentration of traps that can capture the holes. For the first time, it was proposed to take into account the capture of holes by the surface states of  $N_{ts}$  at the metal/Ga<sub>2</sub>O<sub>3</sub> interface in addition to their capture by trap centers in the bulk of the oxide film. The concentration of  $N_{ts}$  depends on the topology of the electrodes, in other words, on the perimeter.

**Author Contributions:** Conceptualization, V.M.K. and A.V.T.; methodology, V.M.K., A.V.T. and A.V.K.; formal analysis, V.M.K., A.V.T. and P.M.K.; investigation, V.M.K., A.V.T., A.V.K. and E.V.Z.; resources, V.M.K., A.V.K. and E.V.Z.; data curation, V.M.K. and A.V.T.; writing—original draft preparation, V.M.K. and A.V.T.; writing—review and editing, V.M.K. and A.V.T.; visualization, V.M.K., P.M.K. and A.V.T.; supervision, V.M.K.; project administration, V.M.K.; funding acquisition, V.M.K. All authors have read and agreed to the published version of the manuscript.

**Funding:** This work was supported by a grant under the Decree of the Government of the Russian Federation No. 220 of 9 April 2010 (Agreement No. 075-15-2022-1132 of 1 July 2022).

**Data Availability Statement:** All data that support the findings of this study are included within the article.

**Conflicts of Interest:** The authors declare no conflicts of interest. The funders had no role in the design of the study; in the collection, analyses, or interpretation of data; in the writing of the manuscript, or in the decision to publish the results.

## References

1. Osipov, A.V.; Sharafudinov, S.S.; Kremleva, A.V.; Osipova, E.V.; Smirnov, A.M.; Kukushkin, S.A. Phase transformations in gallium oxide layers. *Tech. Phys. Lett.* **2023**, *49*, 4–7.
2. Al-Hardan, N.H.; Abdul Hamid, M.A.; Jalar, A.; Firdaus-Raih, M. Unleashing the potential of gallium oxide: A paradigm shift in optoelectronic applications for image sensing and neuromorphic computing applications. *Mater. Today Phys.* **2023**, *38*, 101279. [[CrossRef](#)]
3. Xiao, Y.; Yang, S.; Cheng, L.; Zhou, Y.; Qian, Y. Research progress of solar-blind UV photodetectors based on amorphous gallium oxide. *Opto-Electron. Eng.* **2023**, *50*, 230005.
4. Fei, Z.; Chen, Z.; Chen, W.; Chen, S.; Wu, Z.; Lu, X.; Wang, G.; Liang, J.; Pei, Y.  $\epsilon$ -Ga<sub>2</sub>O<sub>3</sub> thin films grown by metal-organic chemical vapor deposition and its application as solar-blind photodetectors. *J. Alloys Compd.* **2022**, *925*, 166632. [[CrossRef](#)]
5. Yakovlev, N.N.; Nikolaev, V.I.; Stepanov, S.I.; Almaev, A.V.; Pechnikov, A.I.; Chernikov, E.V.; Kushnarev, B.O. Effect of Oxygen on the Electrical Conductivity of Pt-Contacted  $\alpha$ -Ga<sub>2</sub>O<sub>3</sub>/ $\epsilon$ ( $\kappa$ )-Ga<sub>2</sub>O<sub>3</sub> MSM Structures on Patterned Sapphire Substrates. *IEEE Sens. J.* **2021**, *21*, 14636–14644. [[CrossRef](#)]
6. Fornari, R.; Pavesi, M.; Montedoro, V.; Klimm, D.; Mezzadri, F.; Cora, I.; Pécz, B.; Boschi, F.; Parisini, A.; Baraldi, A.; et al. Thermal stability of  $\epsilon$ -Ga<sub>2</sub>O<sub>3</sub> polymorph. *Acta Mater.* **2017**, *140*, 411–416. [[CrossRef](#)]
7. Galazka, Z.  $\beta$ -Ga<sub>2</sub>O<sub>3</sub> for wide-bandgap electronics and optoelectronics. *Semicond. Sci. Technol.* **2018**, *33*, 113001. [[CrossRef](#)]
8. Varshney, U.; Sharma, A.; Vashishtha, P.; Goswami, L.; Gupta, G. Ga<sub>2</sub>O<sub>3</sub>/GaN Heterointerface-Based Self-Driven Broad-Band Ultraviolet Photodetectors with High Responsivity. *ACS Appl. Electron. Mater.* **2022**, *4*, 5641–5651. [[CrossRef](#)]
9. Wang, Y.; Li, S.; Cao, J.; Jiang, Y.; Zhang, Y.; Tang, W.; Wu, Z. Improved response speed of  $\beta$ -Ga<sub>2</sub>O<sub>3</sub> solar-blind photodetectors by optimizing illumination and bias. *Mater. Des.* **2022**, *221*, 110917. [[CrossRef](#)]
10. Almaev, A.; Nikolaev, V.; Kopyev, V.; Shapenkov, S.; Yakovlev, N.; Kushnarev, B. Solar-Blind Ultraviolet Detectors Based on High-Quality HVPE  $\alpha$ -Ga<sub>2</sub>O<sub>3</sub> Films With Giant Responsivity. *IEEE Sens. J.* **2023**, *23*, 19245–19255. [[CrossRef](#)]
11. Polyakov, A.; Nikolaev, V.; Yakimov, E.; Ren, F.; Pearton, S.; Kim, J. Deep level defect states in  $\beta$ -,  $\alpha$ -, and  $\epsilon$ -Ga<sub>2</sub>O<sub>3</sub> crystals and films: Impact on device performance. *J. Vac. Sci. Technol. A* **2022**, *40*, 020804. [[CrossRef](#)]
12. Labeled, M.; Sengouga, N.; Prasad, C.; Henini, M.; Rim, Y. On the nature of majority and minority traps in  $\beta$ -Ga<sub>2</sub>O<sub>3</sub>: A review. *Mater. Today Phys.* **2023**, *36*, 101155. [[CrossRef](#)]
13. Traoré, A.; Okumura, H.; Sakurai, T. Photoconductivity buildup and decay kinetics in unintentionally doped  $\beta$ -Ga<sub>2</sub>O<sub>3</sub>. *Jpn. J. Appl. Phys.* **2022**, *61*, 091002. [[CrossRef](#)]
14. Kananen, B.E.; Giles, N.C.; Halliburton, L.E.; Foundos, G.K.; Chang, K.B.; Stevens, K.T. Self-trapped holes in  $\beta$ -Ga<sub>2</sub>O<sub>3</sub> crystals. *J. Appl. Phys.* **2017**, *122*, 215703. [[CrossRef](#)]
15. Qin, Y.; Long, S.; Dong, H.; He, Q.; Jian, G.; Zhang, Y.; Hou, X.; Tan, P.; Zhang, Z.; Lv, H.; et al. Review of deep ultraviolet photodetector based on gallium oxide. *Chinese Phys. B* **2019**, *28*, 018501. [[CrossRef](#)]
16. Kalygina, V.M.; Tsybalov, A.V.; Almaev, A.; Kushnarev, B.O.; Oleinik, V.L.; Petrova, J.S. Influence of White Light on the Photoelectric Characteristics of UV Detectors Based on  $\beta$ -Ga<sub>2</sub>O<sub>3</sub>. *IEEE Sens. J.* **2023**, *23*, 15530–15536. [[CrossRef](#)]
17. Yang, X.; Du, X.; He, L.; Wang, D. Fabrication and optoelectronic properties of Ga<sub>2</sub>O<sub>3</sub>/Eu epitaxial films on nanoporous GaN distributed Bragg reflectors. *J. Mater. Sci.* **2020**, *55*, 8231–8240. [[CrossRef](#)]
18. Winkler, N.; Wibowo, R.; Kautek, W.; Ligorio, G.; List-Kratochvil, E.; Dimopoulos, T. Nanocrystalline Ga<sub>2</sub>O<sub>3</sub> films deposited by spray pyrolysis from water-based solutions on glass and TCO substrates. *J. Mater. Chem. C* **2019**, *7*, 69–77. [[CrossRef](#)]
19. Lampert, M.A.; Mark, P. *Current Injection in Solids*; Academic Press: New York, NY, USA, 1970; pp. 332–338.
20. Lovejoy, T.C.; Chen, R.; Zheng, X.; Villora, E.G.; Shimamura, K.; Yoshikawa, H.; Yamashita, Y.; Ueda, S.; Kobayashi, K.; Dunham, S.T.; et al. Band bending and surface defects in  $\beta$ -Ga<sub>2</sub>O<sub>3</sub>. *Appl. Phys. Lett.* **2012**, *100*, 181602. [[CrossRef](#)]
21. Ghadi, H.; McGlone, J.F.; Jackson, C.M.; Farzana, E.; Feng, Z.A.; Bhuiyan, U.; Zhao, H.; Arehart, A.R.; Ringel, S.A. Full bandgap defect state characterization of  $\beta$ -Ga<sub>2</sub>O<sub>3</sub> grown by metal organic chemical vapor deposition. *APL Mater.* **2020**, *8*, 021111. [[CrossRef](#)]
22. Wang, Z.; Chen, X.; Ren, F.-F.; Gu, S.; Ye, J. Deep-level defects in gallium oxide. *J. Phys. D Appl. Phys.* **2021**, *54*, 043002. [[CrossRef](#)]
23. Chen, X.; Ren, F.-F.; Ye, J.; Gu, S. Gallium oxide-based solar-blind ultraviolet photodetectors. *Semicond. Sci. Technol.* **2020**, *35*, 023001. [[CrossRef](#)]
24. Hou, X.; Zou, Y.; Ding, M.; Qin, Y.; Zhang, Z.; Ma, X.; Tan, P.; Yu, S.; Zhou, X.; Zhao, X.; et al. Review of polymorphous Ga<sub>2</sub>O<sub>3</sub> materials and their solar-blind photodetector applications. *J. Phys. D Appl. Phys.* **2021**, *54*, 043001. [[CrossRef](#)]
25. Greczynski, G.; Hultman, L. X-ray photoelectron spectroscopy: Towards reliable binding energy referencing, Prog. Mater. Sci. **2020**, *107*, 100591. [[CrossRef](#)]
26. Fares, C.; Ren, F.; Pearton, S.J. Temperature-Dependent Electrical Characteristics of  $\beta$ -Ga<sub>2</sub>O<sub>3</sub> Diodes with W Schottky Contacts up to 500 °C. *ECS J. Solid State Sci. Technol.* **2019**, *8*, Q3007. [[CrossRef](#)]
27. Huan, Y.W.; Sun, S.M.; Gu, C.J.; Liu, W.J.; Ding, S.J.; Yu, H.Y.; Xia, C.T.; Zhang, D.W. Recent Advances in  $\beta$ -Ga<sub>2</sub>O<sub>3</sub>-Metal Contacts. *Nanoscale Res. Lett.* **2018**, *13*, 246. [[CrossRef](#)] [[PubMed](#)]
28. Borelli, C.; Bosio, A.; Parisini, A.; Pavesi, M.; Vantaggio, S.; Fornary, R. Electronic properties and photo-gain of UV-C photodetectors based on high-resistivity orthorhombic  $\kappa$ -Ga<sub>2</sub>O<sub>3</sub> epilayers. *Mater. Sci. Eng. B* **2022**, *286*, 116056. [[CrossRef](#)]
29. Shalimova, K.V. *Semiconductor Physics*; Energy: Moscow, Russia, 1976; pp. 257–262.
30. Guo, D.; Liu, H.; Li, P.; Wu, Z.; Wang, S.; Cui, C.; Li, C.; Tang, W. Zero-Power-Consumption Solar-Blind Photodetector Based on  $\beta$ -Ga<sub>2</sub>O<sub>3</sub>/NSTO Heterojunction. *ACS Appl. Mater. Interfaces* **2017**, *9*, 1619–1628. [[CrossRef](#)] [[PubMed](#)]

31. Kalygina, V.; Podzyvalov, S.; Yudin, N.; Slyunko, E.; Zinoviev, M.; Kuznetsov, V.; Lysenko, A.; Kalsin, A.; Kopiev, V.; Kushnarev, B.; et al. Effect of UV and IR Radiation on the Electrical Characteristics of Ga<sub>2</sub>O<sub>3</sub>/ZnGeP<sub>2</sub> Hetero-Structures. *Crystals* **2023**, *13*, 1203. [[CrossRef](#)]
32. Chen, X.; Xu, Y.; Zhou, D.; Yang, S.; Ren, F.-F.; Lu, H.; Tang, K.; Gu, S.; Zhang, R.; Zheng, Y.; et al. Solar-Blind Photodetector with High Avalanche Gains and Bias-Tunable Detecting Functionality Based on Metastable Phase  $\alpha$ -Ga<sub>2</sub>O<sub>3</sub>/ZnO Isotype Heterostructures. *ACS Appl. Mater. Interfaces* **2017**, *9*, 36997–37005. [[CrossRef](#)] [[PubMed](#)]

**Disclaimer/Publisher's Note:** The statements, opinions and data contained in all publications are solely those of the individual author(s) and contributor(s) and not of MDPI and/or the editor(s). MDPI and/or the editor(s) disclaim responsibility for any injury to people or property resulting from any ideas, methods, instructions or products referred to in the content.